

UC Berkeley

UC Berkeley Previously Published Works

Title

Vascular Microphysiological System for Investigating Endothelial Barrier Function During Organ Preservation and Reperfusion.

Permalink

<https://escholarship.org/uc/item/420383qh>

Journal

Small, 21(11)

Authors

Kim, Yongdeok

Goswami, Ishan

Gill, Elisabeth

et al.

Publication Date

2025-03-01

DOI

10.1002/smll.202410168

Peer reviewed

Vascular Microphysiological System for Investigating Endothelial Barrier Function During Organ Preservation and Reperfusion

Yongdeok Kim, Ishan Goswami, Elisabeth Gill, S. Reza Mahmoodi, Anthony N. Consiglio, Jazmin Velazquez, Gabriel Nieman, Alexis Abigail A. Albuero, Brady Woods, Bradley W. Ellis, Irina Filz von Reiterdank, Korkut Uygun, Basak E. Uygun, Boris Rubinsky, and Kevin E. Healy*

Endothelial cell damage after cold preservation and reperfusion injury causes deterioration of the endothelial barrier and ultimately results in edema, leading to transplant failure. Here, a vascular microphysiological system (MPS) is introduced as a testbed to investigate the combinational effect of thermal and fluid perturbations (i.e., wall shear stress) on human endothelial barrier function. Two methods of organ storage are compared: isochoric supercooling (ISC) preservation, which prevents ice formation at subzero temperatures; and, the standard clinical protocol of static cold storage (SCS) at 4 °C. Integrating electrical impedance measurements on chip allow real-time monitoring and quantification of barrier function during preservation and reperfusion protocols. Isochoric supercooling preservation enables longer periods of preservation with superior recovery of barrier function during reperfusion, and has lower metabolic activities compared to static cold storage. Genomic analysis reveals injury and recovery mechanisms at the molecular level for the different preservation and reperfusion conditions. The multifunctional vascular microphysiological system provides a physiologically relevant *in vitro* model recapitulating ischemia-reperfusion injury to the endothelium. The vascular MPS has potential for optimizing organ preservation protocols, ultimately improving organ transplant viability.

1. Introduction

Over the past decades, the demand for organ transplantation has grown rapidly with supply unable to keep pace.^[1,2] A significant bottleneck in expanding patient access to organ transplantation is limited preservation times with the current clinical standard of static cold storage (SCS) capable of storing organs on the time scale of hours (4–6 h for heart and vascularized composite allografts (VCA), 8 h for lung, 12 h for liver, and 24 h for kidney).^[3–5] This allows for only regional sharing of organs while preventing use of new techniques such as mixed-chimerism based tolerance induction, resulting in inequitable organ allocation.^[5–8] One such remedy to this logistical bottleneck is the use of extended preservation strategies, which have shown the potential to increase the scale of organ preservation to days or even months.^[9–17] The clinical implementation of such protocols would improve allocation, reduce logistical costs and constraints, and facilitate comprehensive immunological matching to improve patient outcomes.

 The ORCID identification number(s) for the author(s) of this article can be found under <https://doi.org/10.1002/sml.202410168>

[+]Present address: Department of Electrical and Computer Engineering, University of Denver, Denver, CO 80208, USA

[++]Present address: Biomaterials Research Center, Korea Institute of Science and Technology (KIST), Seoul 02792, South Korea

[Correction added on February 20, 2025, after first online publication: Name of I.F.R. has been corrected.]

© 2025 The Author(s). Small published by Wiley-VCH GmbH.

This is an open access article under the terms of the [Creative Commons Attribution-NonCommercial-NoDerivs](#) License, which permits use and distribution in any medium, provided the original work is properly cited, the use is non-commercial and no modifications or adaptations are made.

DOI: 10.1002/sml.202410168

Y. Kim^[++], I. Goswami, E. Gill, S. R. Mahmoodi^[+], J. Velazquez, G. Nieman, A. A. A. Albuero, B. Woods, B. Rubinsky, K. E. Healy
Department of Bioengineering and California Institute for Quantitative Biosciences (QB3)
University of California
Berkeley, CA 94720, USA
E-mail: kehealy@berkeley.edu

Y. Kim^[++], I. Goswami, S. R. Mahmoodi^[+], K. E. Healy
Department of Materials Science and Engineering
University of California
Berkeley, CA 94720, USA
A. N. Consiglio, B. Rubinsky
Department of Mechanical Engineering
University of California
Berkeley, CA 94709, USA

Recent advances in machine perfusion and biopreservation techniques have significantly extended the storage durations for organs such as the liver, heart, kidney, pancreas, and VCA.^[9–19] Lowering storage temperatures (T) to suppress metabolic activity, approaches such as supercooling ($0 < T < -10$ °C),^[12,13,20–24] partial freezing ($-10 < T < -20$ °C),^[14] and vitrification ($T < -130$ °C)^[15,16,25] have enabled preservation times to increase from days to months. However, these techniques are limited by their reliance on cryoprotective agents (CPA) to prevent or control ice nucleation during subzero temperature storage.^[12–14] Vitrification, in addition, potentially requires metal nanoparticles to facilitate rapid and uniform warming.^[15,16] Despite their efficacy in preserving organs for extended periods, the toxicity of CPAs and nanoparticles, alongside the need for specialized re-warming equipment, poses significant challenges for clinical translation.^[26,27] In contrast, isochoric supercooling (ISC) offers a method to stabilize the supercooled liquid state without the need for melting point depressing CPAs. Isochoric (constant volume) confinement isolates the aqueous system from external perturbations as well as provides a kinetic resistance to the initial ice nucleus formation, thereby enabling ice-free preservation at subzero temperatures without chemical modulation.^[20,28] This approach potentially circumvents the limitations of other methods, isolating the metabolism suppressing benefits of subzero temperatures by enabling scalable supercooling using standard hypothermic storage solutions.

A main challenge facing preservation techniques is ischemia-reperfusion injury (IRI), a primary cause of preservation damage in organs, critically involving the endothelium. The endothelium serves as the initial barrier to both the introduction of organ storage solutions and subsequent reperfusion post-transplantation. The semi-permeable barriers in vasculature serve to control two-way transport including small and macromolecules, gases, and immune cells.^[29] Endothelial dysfunction during preservation and reperfusion is thought to be a key factor in the damage occurring in transplanted organs by showing severe edema in transplantation, which can ultimately result in transplant failure.^[10,30,31] However, a more physiologically relevant model is required to understand the mechanism of damage and recovery of endothelial barrier function during preservation and reperfusion at cellular and molecular levels. Although animal models provide insights by assessing endothelial damage through analyzing gross parameters such as vascular resistances and weight changes as well as histology, they are limited by their non-human nature and investigating endothelial barrier function at the organ level.^[10,17,30,32] While some in vitro models have been utilized to observe the effects of low-temperature preservation on endothelial cells (ECs), they lack dynamic flow thereby diminishing their physiological applicability.^[32–34] 2D cell culture models in static conditions are limited and do not recapitulate vascular systems. For example, physiologically relevant fluid wall shear stress (WSS) is known to be critical to maintaining endothelial phenotype and functions.^[29,35–37]

3D microphysiological systems (MPS) have been validated as potent human-based physiologically relevant testbeds for biopreservation, ischemia-reperfusion, and vascular disease modeling studies prior to ex vivo and in vivo models.^[20,33,37–39] Our previous work used this technology to develop a microfluidic human cardiac MPS to demonstrate the revival of human induced pluripotent stem cell-derived cardiac microtissues after 3–4 days of ISC preservation.^[20] In the context of the vasculature, such devices could recapitulate vascular systems with responsive barrier function and physiologically relevant WSS.^[29,35,36,39,40] Furthermore, integrating sensors within a vascular MPS such as electrical impedance spectroscopy (EIS) and transepithelial electrical resistances (TEER) measurement can allow for real-time monitoring of endothelial barrier function on chip.^[40,41] Furthermore, those techniques provide quantitative and non-invasive assessment of endothelial barrier integrity through an equivalent circuit model without disturbing the cells. However, to our knowledge, no study has reported the effect of preservation protocol damage on endothelial barrier function for low temperature preservation and reperfusion conditions with physiologically relevant WSS. Investigating the combined effects of thermal and fluidic perturbations on a chip is critical to recapitulate the IRI on endothelium and assess barrier function during the preservation and reperfusion.

Here, we introduce a 3D vascular MPS testbed for the study of organ preservation to investigate the combinational effects of temperature and WSS perturbations on human endothelial barrier function. The microfluidics channel, based on finite element analysis, provides variable WSS to recapitulate mature human arteries allowing us to observe endothelial cell injury and recovery during reperfusion after preservation. Integrating EIS sensors into the MPS enabled real-time monitoring and quantification of endothelial barrier function under different preservation protocols, such as SCS at 4 °C and ISC at –3 °C. Furthermore, genomic analysis revealed the biological pathways involved in endothelial injury and recovery during preservation and reperfusion.

2. Results

2.1. Vascular MPS Modeling and Fabrication

Leveraging computational modeling and microfabrication techniques, the vascular MPS was designed and fabricated to quantitatively sense changes in the endothelial barrier through EIS as well as physiological relevance via WSS. The microfluidic PDMS chip was constructed via photolithography and replica molding (Figure S1, Supporting Information) and was seamlessly bonded to the sensor substrate through oxygen plasma treatment (Figure 1A). To monitor endothelial monolayer function, interdigitated gold electrode arrays (40 μm width) (Figure S2, Supporting Information) were fabricated on the glass substrate with photolithography and etching. The four separated electrode arrays were positioned at regions of different WSS within the cell chamber of the microfluidic MPS (Figure 1B).

Variable WSS ranging from venous (1–5 dynes cm^{–2}) to arterial (>7 or 10 dynes cm^{–2}) levels was designed based on the finite element analysis with COMSOL modeling (Figure 1C).^[29,42] For a specific volumetric flowrate (Q), the tapered cell chamber design created a linear WSS gradient via changes in fluid velocities

B. W. Ellis, I. Filz von Reiterdank, K. Uygun, B. E. Uygun
Center for Engineering in Medicine and Surgery
Massachusetts General Hospital
Harvard Medical School and Shriners Children's Boston
Boston, MA 02114, USA

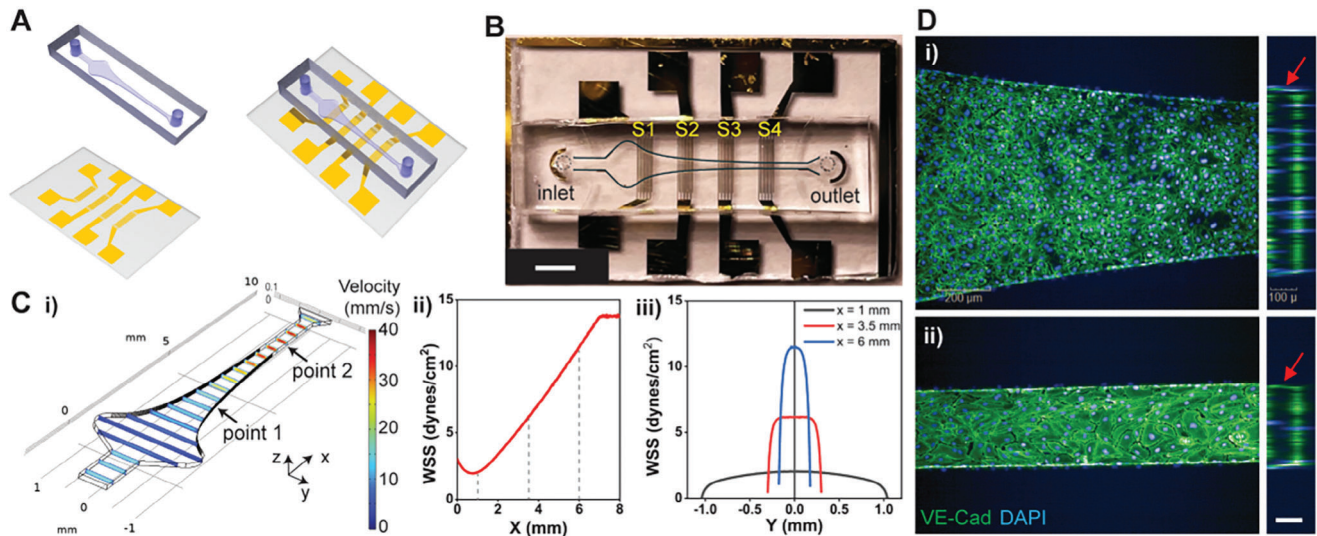


Figure 1. 3D vascular MPS with variable wall shear stress (WSS) outfitted for electrical impedance spectroscopy (EIS). A) Schematic of PDMS MPS assembly with the electrode arrays positioned along the X-axis. B) Photograph of vascular MPS instrumented with 40 μm width electrodes S1 through S4 at 4 regions within the tissue chamber at different wall shear stresses. Outline of cell chamber is marked with fiduciary black lines. Scale bar: 1 mm. C) Finite element analysis using COMSOL modeling showing: i) fluid velocity profiles in the tapered cell chamber; ii) WSS along the X-axis at $Y = 0$; and, iii) Y-axis WSS at $X = 0.5, 3.5,$ and 6.5 mm with a media volumetric flowrate (Q) of $40 \mu\text{L min}^{-1}$. The dotted lines in ii) correspond to $X = 1, 3.5,$ and 6 mm. D) Confocal immunofluorescence images of human coronary artery ECs within the cell chamber of the vascular MPS. ECs organize according to shear stress: i) at **point 1** in Ci, low shear stress cells are disorganized; and, ii) at **point 2** in Ci, high shear stress cells are aligned with flow and have larger volume. Images on the right (red arrows) demonstrate ECs cover the surface area of the cell channel, clearly developing a 3D open lumen. VE-Cadherin (green) and nuclei (DAPI/blue). Scale bar: $100 \mu\text{m}$.

that were dependent on the chamber cross-sectional area.^[43,44] Figure 1C shows: i) fluid velocity profiles in the tapered cell chamber for media with a volumetric flow rate of $40 \mu\text{L min}^{-1}$. ii) The WSS gradient in the direction of fluid flow (x-axis) ranged from 2 to $14.2 \text{ dynes cm}^{-2}$, with linearity from the widest (2.3 mm) to the narrowest (0.3 mm) channel widths. The MPS geometry models arterioles and therefore, employs laminar flow modeling due to the higher aspect ratio and Reynolds number compared to Hele-Shaw flow. Figure 1C-ii confirms that this laminar flow assumption maintains WSS linearity with minimal deviation compared to Hele-Shaw flow, as validated in Figure S3A (Supporting Information). Additionally, the WSS profile along the Y-axis at different channel widths was calculated (Figure 1C-iii). Additional modeling demonstrated higher fluid velocity and WSS profiles with the linear trend along the fluid direction ranging from 3.5 to $24.5 \text{ dynes cm}^{-2}$ when a volumetric flowrate of $70 \mu\text{L min}^{-1}$ was used (Figure S3B–D, Supporting Information). These results show that the tapered microfluidic channel covers a broad range of WSS spanning venous to arterial vessels.

2.2. Human Artery ECs Morphology and State Depend on WSS

Human coronary artery ECs within cell chamber exhibit a 3D lumen structure surrounding the channel surface (Figure 1D; Video S1, Supporting Information). The variable WSS elicited notable alteration in artery ECs morphology and expression in vascular endothelial growth factor receptor 3 (VEGFR3) (Figure 2). VEGFR3 was used as a vascular remodeling marker depending on WSS.^[45] The microfluidics setup (Figure S4, Supporting Information), incorporated features such as switching func-

tionality, fluid sensor, and pressure-driven pumps, enabling sustained perfusion at elevated flow rates while minimizing reperfusion media waste during long culture periods. With $Q = 40 \mu\text{L min}^{-1}$ the WSS ranged from 2 to $14.2 \text{ dynes cm}^{-2}$, where different WSS levels led to distinct EC morphologies characterized by differences in size, eccentricity, alignment, and VEGFR3 expression (Figure 2A,B). Notably, smaller and circular EC shapes were observed for WSS of 3 dynes cm^{-2} , contrasting with the larger and elongated morphologies observed for $14.2 \text{ dynes cm}^{-2}$ (Figure 2A-i,B-i).

Further analysis involved categorizing the cell chamber into three distinct WSS regions based on COMSOL modeling (Figure S3E, Supporting Information), facilitating quantitative assessment of EC morphologies including those not subjected to flow but in the same position of MPS channel (Figures S5 and S6, Supporting Information). We observed a trend toward larger cell size, increased eccentricity (greater elongation), and alignment with the fluid direction at WSS levels exceeding 8 dynes cm^{-2} (Figure 2C–E). Moreover, increased VEGFR3 expression, known as a flow-dependent vascular remodeling marker, increased with WSS (Figure 2F).^[45] These results underscore the capacity of elevated WSS, akin to arterial conditions, to prompt artery-like EC morphologies and functional attributes in the vascular MPS, consistent with prior reports.^[46,47]

2.3. EIS Measurement and Quantification for Endothelium Barrier Resistance

The integration of electrodes into the MPS facilitated monitoring and quantifying endothelial barrier function via EIS.

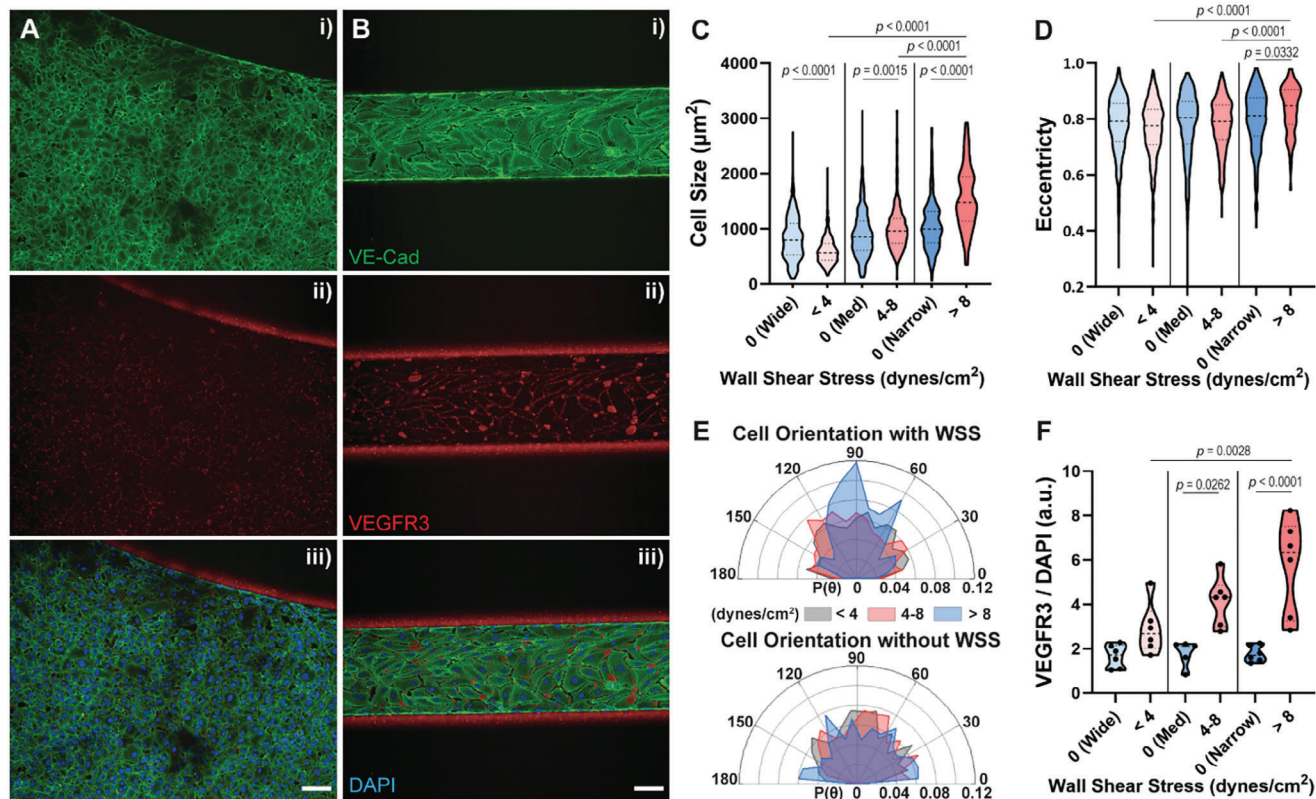


Figure 2. Morphological and functional changes in human artery ECs with variable WSS. Immunofluorescence images of ECs within the cell chamber of the vascular MPS with WSS of A) ≈ 3 dyne cm^{-2} and B) 14.2 dyne cm^{-2} ($Q = 40 \mu\text{L min}^{-1}$; 6h): i) VE-Cadherin (Green); ii) VEGFR3 (Red); and iii) merged images nuclei (DAPI/Blue). Scale bars: $100 \mu\text{m}$. C) Cell size, D) eccentricity of single cells, E) angular histology for cell orientation, and F) VEGFR3 expression normalized by DAPI for different WSS regions and the same areas without flow (static). One way ANOVA followed by Tukey's post-hoc multiple comparisons was used for multigroup analysis. At least four independent MPS replicates were used for EC morphological analysis in C-E and three for VEGFR3 expression analysis in F.

Figure 3A shows increased impedance bode plots following EC loading compared to bare electrodes before seeding them at the narrow channel. The $|Z|$ increased for most frequencies relative to the bare electrodes as ECs formed a monolayer on the electrodes and functioned as insulators. However, $|Z|$ decreased right after cold preservation SCS because the barrier function between ECs weakened. EC covered $|Z|$ values exhibit consistent trends across all four electrode pairs at different channel widths, with the maximum peak sensitivity observed at 15 kHz (**Figure 3B**). These sensitivity patterns and values align with those of commercial EIS platforms.^[41] Although the sensitivity averages for S1 and S2 are higher than S3 and S4, due to the larger exposed electrode areas, the differences were insignificant (**Figure S7A,B**, Supporting Information).

The EIS-integrated vascular MPS enabled real-time sensing of the endothelium during cell loading, preservation, and reperfusion. Based on the impedance sensitivity (**Figure 3B**), 15 kHz was used for the temporal EIS measurements. Rapid impedance increase for all electrode pairs on chip was observed within the initial 10 min post-cell loading, plateauing ≈ 20 min (**Figure S7C**, Supporting Information). Corresponding images of EC coverage on the MPS channel (**Figure S7D,E**, Supporting Information) reflected these impedance trends. Additionally, EIS measurement enabled monitoring of EC behavior during cold

preservation. SCS (24 h at $4 \text{ }^\circ\text{C}$) caused a decline of $|Z|$ (**Figure S7F**, Supporting Information) caused by uneven cellular boundaries and deterioration of endothelium (**Figure 3A**, inset). The equivalent circuit model was employed to quantify tight junction resistances (R_{TJ}), an indicator of endothelial barrier function (**Figure 3C**). Classical models were modified to include a constant phase element to improve fitting (**Figure S8**, Supporting Information).^[41,48] We quantified cellular components of the model, including R_{TJ} , membrane capacitance (C_{MEM}), and cytoplasmic resistance (R_{CYT}). These measurements results highlight the sensing capabilities of vascular MPS for real-time monitoring and quantification of endothelial barrier function with EIS.

2.4. Barrier Function During SCS and ISC for 24–96 H

The vascular MPS with EIS was used to monitor changes in the endothelium after SCS and ISC preservation protocols. **Figure 4A** depicts the SCS and ISC biopreservation protocols, including temperature and time curves. A unique feature of ISC is that it employs volume confinement within a customized aluminum chamber for metastable supercooled storage (**Figure 4B**). The pressure sensor on the chamber enables monitoring of

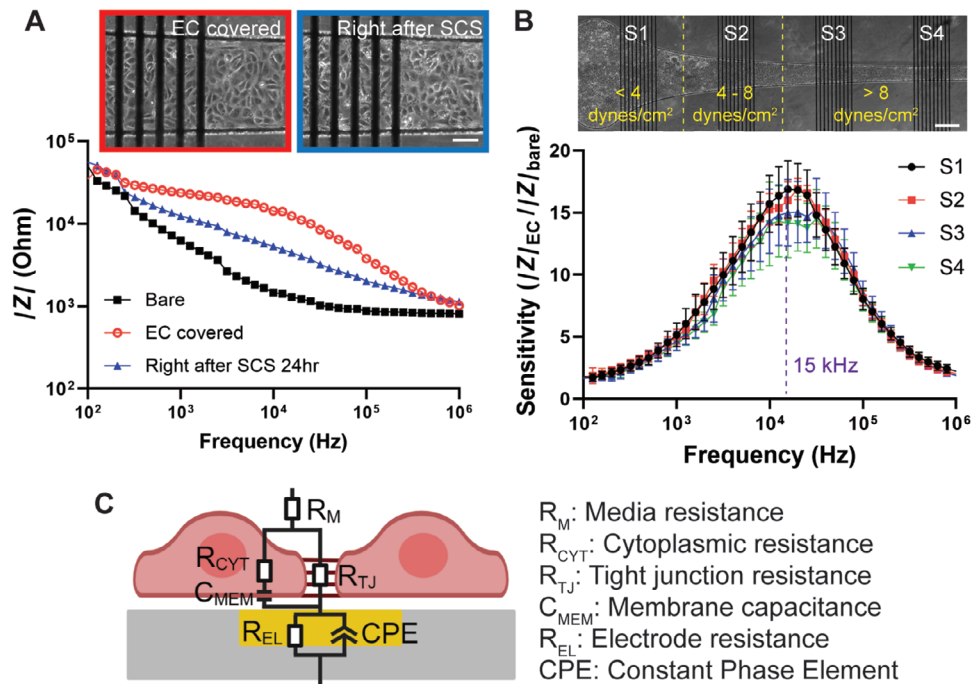


Figure 3. EIS measurement on vascular MPS. A) Impedance bode plots for a bare electrode, EC-covered electrode, and after SCS for 24 h. Brightfield images show the ECs over the electrodes (Top). Scale bar: 100 μ m. B) Frequency dependence (100 Hz to 1 MHz) of sensitivity ($|Z|_{EC} / |Z|_{bare}$) for EC-covered electrodes. Brightfield images show electrodes pairs corresponding to the WSS on the tapered channel (Top). Data were expressed as mean \pm standard deviation. Scale bar: 500 μ m. At least five independent MPS replicates were used for EIS sensitivity analysis. C) Equivalent circuit model of ECs on electrode with nomenclature.

pressure changes during preservation, which can indicate ice nucleation. Representative impedance bode plots before and immediately post-SCS and ISC, and after 4 h of reperfusion demonstrate decreases in $|Z|$ immediately post-preservation, with recovery occurring only with the ISC protocol (Figure S9, Supporting Information). Figure 4C–J presents R_{TJ} prior to preservation, immediately post-preservation, and after 4 h of reperfusion for SCS and ISC for durations of 24, 48, 72, and 96 h. Immediately post-preservation R_{TJ} significantly decreased, for both SCS and ISC, compared to before cold storage. Reperfusion led to the recovery of R_{TJ} to levels like those before preservation for 24 h of SCS and 24–96 h of ISC, although some variations exist in the reperfusion for 48–96 h. To account for these variations after reperfusion, p -values were assessed between before preservation and after reperfusion (Figure 4K). No significant differences were observed between before preservation and after reperfusion for 24 h of SCS and 24–96 h of ISC. For SCS longer than 48 h, R_{TJ} failed to recover during reperfusion ($p = 0.0045$, < 0.0001 , and < 0.0001 for 48, 72, and 96 h of SCS, respectively). Longer SCS caused larger drops in normalized R_{TJ} during reperfusion: 0.878, 0.652, 0.179, and 0.149 (medians) for 24, 48, 72, and 96 h duration of SCS (Figure 4C–F). ISC showed significantly better recovery of R_{TJ} during reperfusion for durations of 24–96 h storage (Figure 4G–J). The R_{TJ} after reperfusion for ISC durations of 24, 48, 72, and 96 h were 0.994, 1.005, 0.867, and 0.863 (medians). Real-time monitoring of $|Z|$ during reperfusion showed recovery within an hour for ISC durations < 96 h but took ≈ 3 h to recover for 96 h of storage; however, SCS endothelium never recovered, except for 24 h of storage (Figure 4L,M).

Figure 5 highlights the differences between SCS and ISC. Figure 5A,B present normalized R_{TJ} immediately post-preservation and after reperfusion in SCS and ISC for 24–96 h. The median values immediately after SCS for 24, 48, 72, and 96 h are 0.425, 0.214, 0.160, 0.139, respectively. R_{TJ} immediately post-SCS dropped with longer preservation times, showing significant differences compared to the 24 h of SCS. Figure 5C–E shows the actin filament disassembly during SCS. Disconnected and dotted actin filaments during SCS caused cell shrinkage and loosely bound cell-cell junctions, resulting in the reduced R_{TJ} . Longer SCS led to larger spaces between ECs in Figure 5E compared to Figure 5D due to these phenomena. Figure 5F shows a fewer number of ECs remaining after reperfusion in 96 h of SCS because the loosely bound cells detached and washed out during reperfusion, corresponding to the decreasing trend in R_{TJ} after reperfusion of SCS (Figure 5B).

R_{TJ} immediately post-ISC for 24 h showed a larger drop compared to the 24 h of SCS. Figure 5G immediately after 24 h of ISC presents larger gaps between ECs compared to Figure 5D immediately after 24 h of SCS. However, R_{TJ} after reperfusion in ISC showed more recovery than SCS, especially after 72 and 96 h of preservation (Figure 5B). The p values in R_{TJ} after reperfusion between SCS and ISC for 72 and 96 h of preservation are 0.0017 and below 0.0001, respectively. Figure 5H shows larger gaps between ECs and disassembled actin filaments immediately post-ISC. In contrast, Figure 5I demonstrates recovery, with smaller gaps and restored actin filament assembly within cells. The bright field images of ECs on MPS immediately post-SCS and ISC for 24–96 h

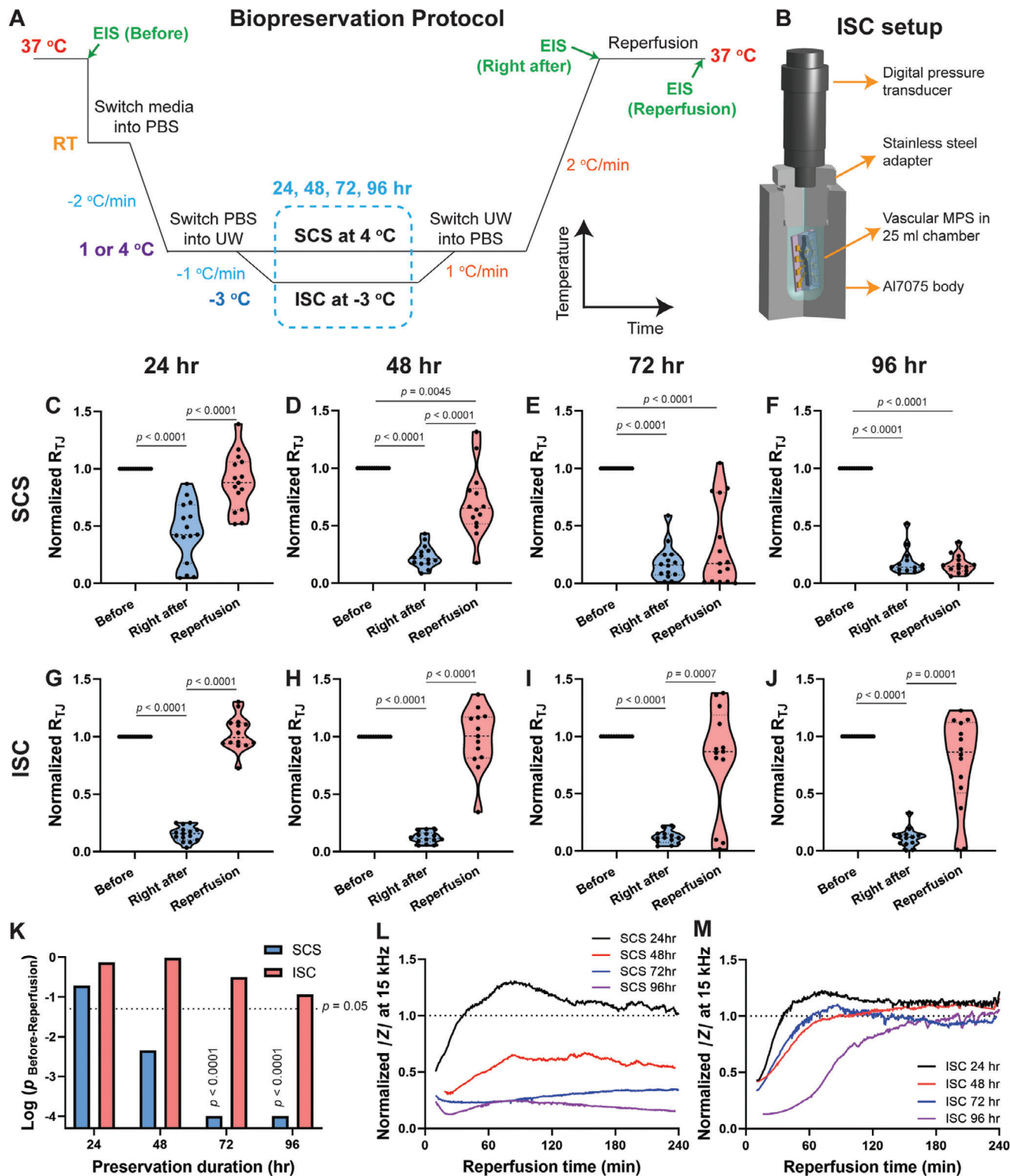


Figure 4. EIS results of vascular MPS in preservation and reperfusion. A) Time-temperature schematic for biopreservation SCS and ISC. B) Schematic of the ISC device. Violin plots for R_{TJ} (normalized to before preservation) for immediately post-preservation and after 4h reperfusion of the vascular MPS for SCS for C) 24, D) 48, E) 72, and F) 96 h, and ISC for G) 24, H) 48, I) 72, and J) 96 h. K) Statistically significant differences between before preservation and after reperfusion for SCS and ISC for durations 24–72 h. Data analyzed from C–J. Dotted line indicates $p = 0.05$. Temporal normalized $|Z|$ during reperfusion after (L) SCS and (M) ISC for 24, 48, 72, and 96 h of storage. One way ANOVA followed by Tukey's post-hoc multiple comparisons was used for multigroup analysis. At least four independent MPS replicates were used for EIS results with biopreservation in C–K.

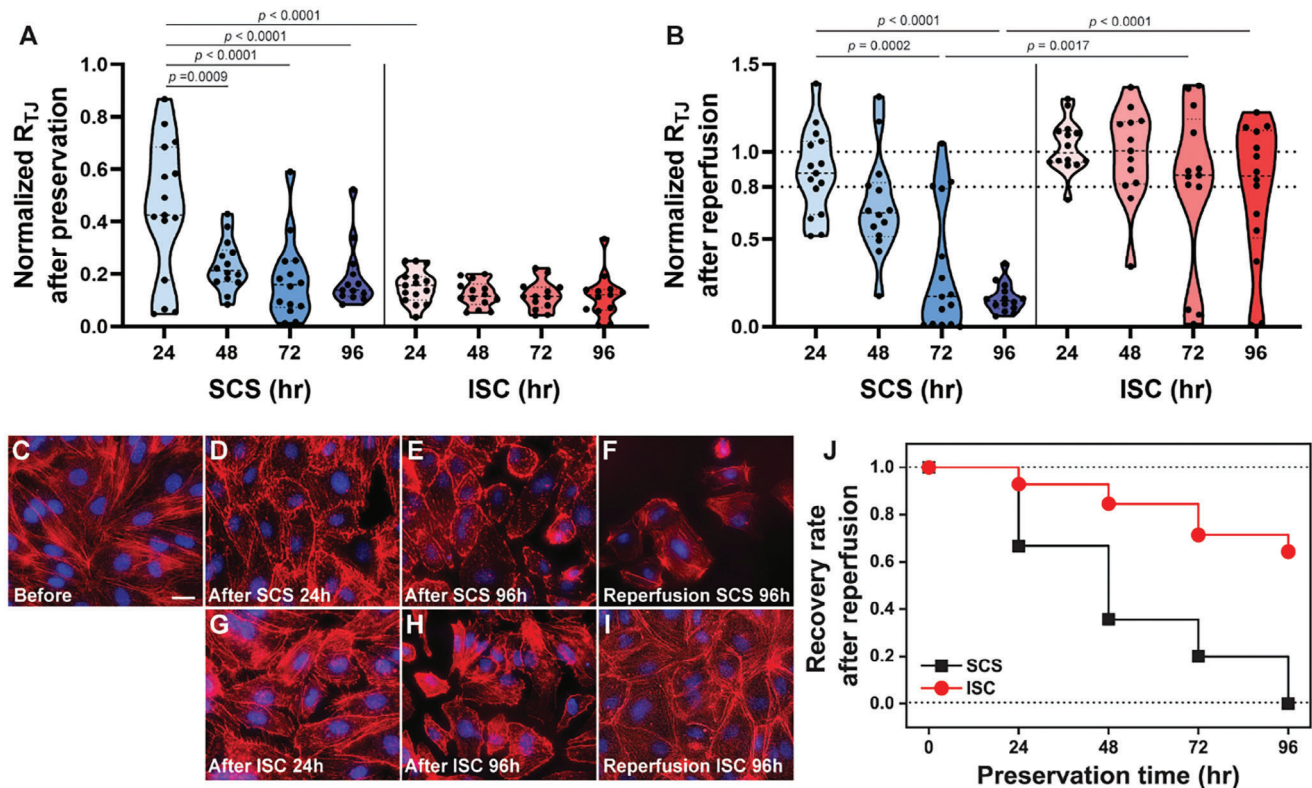


Figure 5. Comparison of SCS and ISC biopreservation protocols. A) Normalized R_{TJ} immediately post-SCS and -ISC for 24, 48, 72, and 96 h of storage. B) Normalized R_{TJ} after reperfusion for 4 h after SCS and ISC for 24, 48, 72, and 96 h of storage. Dotted lines indicate 80% and 100% of normalized R_{TJ} after reperfusion. (A) and (B) were replotted from Figure 4C–J. Immunofluorescence images for F-actin (phalloidin, red) and nuclei (DAPI, blue) C) before preservation and immediately post-SCS for D) 24 and E) 96 h, and F) after 4 h of reperfusion in 96 h of SCS. Immunofluorescence images for F-actin (phalloidin, red) and nuclei (DAPI, blue) immediately post-ISC for G) 24 and H) 96 h, and I) after 4 h of reperfusion in 96 h of ISC. Scale bar: 20 μm . J) Barrier R_{TJ} recovery rate after reperfusion for SCS and ISC for 24, 48, 72, and 96 h. One way ANOVA followed by Tukey's post-hoc multiple comparisons was used for multigroup analysis.

and after reperfusion showed the same trend in Figure S10 (Supporting Information).

ISC showed a better recovery rate after 4 h of reperfusion for 24–96 h of preservation than SCS in Figure 5J. Recovery rates (over 80% of normalized R_{TJ} after reperfusion from Figure 5B) for both SCS and ISC reduced with longer preservation periods, though ISC was higher than SCS all the time. Particularly, in longer preservation such as 72 and 96 h, the recovery rates for SCS are 0.2 and 0, while those for ISC are 0.69 and 0.64. To compare between frozen and supercooled preservation at the same temperature, some samples were stored frozen at $-3\text{ }^{\circ}\text{C}$ for 96 h and measured with EIS (Figure S11, Supporting Information). These samples failed to recover barrier function after reperfusion, similar to the SCS samples preserved for 96 h.

The variable WSS MPS also allows the characterization of the barrier function and recovery rates in preservation and reperfusion depending on the WSS (Figures S12 and S13, Supporting Information). Figure S12 (Supporting Information) presents R_{TJ} with WSS immediately post-SCS and ISC for 24–96 h, normalized to before preservation. No trends in R_{TJ} depending on WSS were observed due to the static storage of chips, without flow, for both SCS and ISC. Figure S13 (Supporting Information) shows R_{TJ} and recovery rates with WSS after 4 h of reperfusion in SCS and ISC for 24–96 h, normalized to before preservation. No sig-

nificant differences were observed in R_{TJ} depending on WSS after reperfusion for both SCS and ISC (Figure S13A,B, Supporting Information). However, the recovery rate after reperfusion in Figure S13C indicates lower recovery rates in higher WSS ($>8\text{ dynes cm}^{-2}$) for 24–96 h of SCS. In 24 h of SCS, recovery rates for lower WSS ($<4\text{ dynes cm}^{-2}$) and 4–8 dynes cm^{-2} were 1.00 and 0.75, while they decreased drastically to below 0.25 after 48 h of SCS. Although $>75\%$ of chips in lower than 8 dynes cm^{-2} were recovered after reperfusion in 24 h of SCS, only 43% of those in $>8\text{ dynes cm}^{-2}$ showed recovery of barrier function. For recovery rates in ISC depending on WSS in Figure S13D (Supporting Information), generally, it was difficult to find any correlation between WSS and recovery rates. Only WSS higher than 8 dynes cm^{-2} in 96 h of ISC showed lower recovery rates than 50%, while other conditions had $>60\%$ recovered barrier function.

2.5. Transcriptomic Analysis after SCS and ISC

Transcriptomic analysis was used to assess molecular level differences in the endothelium for SCS and ISC protocols. Since 96 h of preservation showed the largest significant difference between SCS and ISC after reperfusion (Figure 5B), we

further explored these conditions with mRNA sequencing. Immediately after preservation, larger differences in overall mRNA expression was observed for ISC than SCS compared to before preservation (Figure 6A,B). Immediately post-ISC for 96 h, proinflammatory response-related mRNAs such as CXCL2, CXCL3, SELE, and CSF3 were significantly upregulated, while metabolism-related markers including MSMO1 and HMGCS1 were downregulated (Figure 6B). BOLA2B was downregulated for both immediately post-SCS and -ISC. As BOLA proteins are involved in iron metabolism and strongly correlate with an aerobic metabolism, the downregulation of BOLA2B gene may be caused by the hypoxia condition during preservation for both SCS and ISC.^[49]

During reperfusion, unfolded protein responses and responses to heat were significantly upregulated for both ISC and SCS compared to immediately post-preservation, including HSPA6, HSPA7, HSPA1A, HSPA1B, and CYRAB (Figure 6C,D). Similar results were observed comparing reperfusion for SCS and ISC for 96 h to controls without preservation (Figure S14, Supporting Information), although more significant upregulation in HSPA6, HSPA1A, and HSPA1B were observed. More significant upregulation was observed for ISC compared to SCS preservation. In addition, inflammatory response-related markers were significantly altered during reperfusion in SCS (Figure 6C), where CXCL2, CD83, CXCL3, IL1A, and EGOT, were upregulated compared to immediately post-SCS. Meanwhile, CXCL2 was downregulated after reperfusion for ISC (Figure 6D). There were different trends in inflammation-related pathways based on KEGG enrichment analysis between SCS and ISC, including MAPK signaling, NF-kappa B signaling, IL-17 signaling, TNF signaling pathways, and cytokine-cytokine receptor interaction (Figure S15A, Supporting Information). In the case of SCS, although no significant upregulation in these pathways was shown immediately after preservation, they were significantly upregulated during reperfusion. In the case of ISC, significant changes were observed immediately after preservation, while no significant upregulation was observed during reperfusion compared to immediately post-ISC. The heat map for cytokine-cytokine receptor interaction, indicated higher expression immediately post-ISC and after reperfusion in SCS compared to other conditions (Figure S15B, Supporting Information).

Enrichment results based on gene ontology immediately post-preservation and after reperfusion were focused on the metabolic processes and protein folding (Figure 6E,F). Significant downregulation of metabolic processes was more prevalent for ISC treated endothelium compared to SCS, including cholesterol, steroid, secondary alcohol, sterol, neutral lipid, acylglycerol, organic hydroxy compound, and triglyceride. Heat maps for mRNA expression related to cholesterol, fatty acid, and glucose metabolic processes showed greater downregulation of markers immediately post-ISC compared to SCS (Figure 6G), a result anticipated since the lower temperature in ISC can suppress metabolic activities during preservation. Figure 6F,H also support the higher statistical significance in ISC than SCS, including response to topologically incorrect protein, response to unfolded protein, protein refolding, 'de novo' posttranslational protein refolding, response to heat, cellular response to heat, response to temperature stimulus. Figure S16 (Supporting Information) shows the

closed relations on those pathways involved in unfolded protein responses and responses to heat. Finally, upregulation of mRNA related to apoptosis and oxidative stress was most prevalent in the reperfusion SCS protocol (Figure 6I; Figure S17, Supporting Information).

3. Discussion

In this study, a multifunctional vascular MPS was used to evaluate organ preservation protocols using SCS at 4 °C and ISC at -3 °C. ISC allows the storage of biological systems at subzero temperatures without ice formation or CPA, potentially extending organ storage by suppressing metabolic activity. Our workflow included a vascular MPS that employed variable WSS, immunofluorescent microscopy, and EIS, which allowed real-time monitoring and quantification of endothelial barrier function during preservation and reperfusion protocols. EC barrier resistance dropped immediately post-SCS and ISC, and recovered during reperfusion for 24 h of storage for both protocols, but only ISC demonstrated recovery after 48–96 h of storage. Under such storage conditions, a damaged endothelium with the basal membrane directly exposed to blood flow may lead to edema in clinical settings. Thus, ISC showed better recovery of barrier resistance during reperfusion compared to SCS for extended preservation durations. Combining the vascular MPS with transcriptomic analysis revealed recovery and failure mechanisms in SCS and ISC related to metabolic activities, inflammatory responses, and unfolded protein response. Collectively, we demonstrated longer preservation capabilities for ISC compared to SCS, with better recovery of barrier function, identified potential pathways to target for improving preservation, and the potential of ISC as clinical protocol for organ preservation.

There were salient differences in the endothelium response to SCS and ISC preservation. During reperfusion, barrier R_{TJ} with ISC showed better recovery rates than SCS, especially after 72 and 96 h of preservation (Figure 5B,J). The endothelial damage during ISC activated unfolded protein responses during reperfusion, resulting in the restoration of endoplasmic reticulum and recovery of endothelial barrier function. Unfolded protein responses are known to restore protein homeostasis or direct cells to apoptosis.^[50,51] The recovery of barrier R_{TJ} , along with the significant upregulation in unfolded protein responses following reperfusion with ISC, suggests restoration of homeostasis rather than apoptosis. Meanwhile, SCS provided lower recovery rates in barrier R_{TJ} after reperfusion (Figure 5J), with significant decreases observed after reperfusion following longer than 48 h of SCS (Figure 4D–F). As IRI is known to induce proinflammatory responses, SCS was more vulnerable to IRI during reperfusion compared to ISC preservation.^[52,53] Greater upregulation in inflammatory responses, an IRI indicator, after reperfusion in SCS supports the failure of barrier resistance. Although upregulation in unfolded protein responses was shown after reperfusion in SCS, it may be related to apoptosis rather than restoration of homeostasis. Higher mRNA expression in apoptosis and cellular response to oxidative stress after reperfusion in SCS support this mechanism (Figure 6I; Figure S17, Supporting Information).

The EIS and transcriptomic analysis results highlight how ISC can offer longer preservation durations (i.e., days) compared to SCS in terms of EC barrier function and molecular changes by

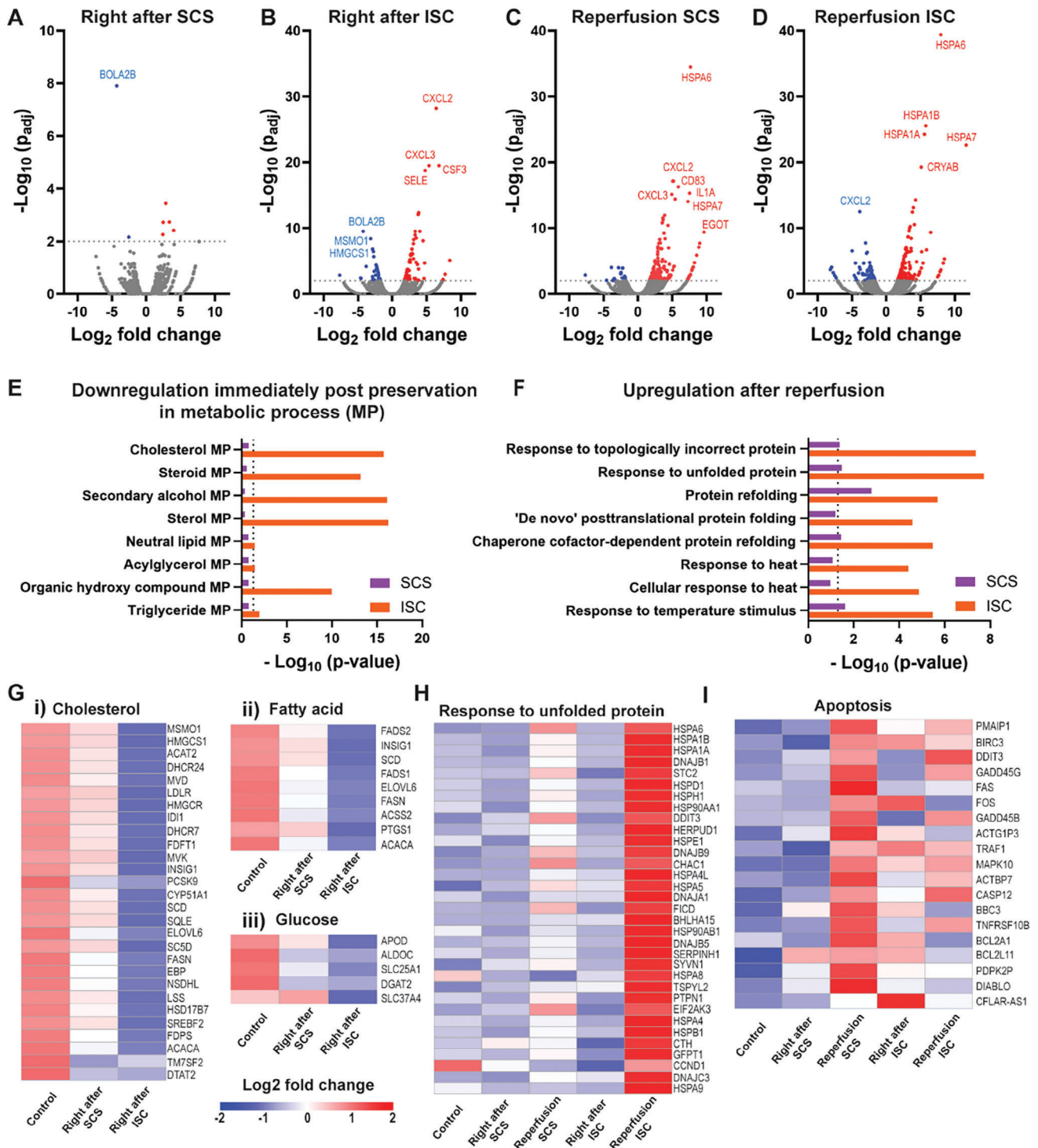


Figure 6. Transcriptomic analysis of SCS and ISC protocols immediately after storage and after reperfusion. Volcano plots for comparing (A) immediately post-SCS for 96 h and control before preservation, and (B) immediately post-ISC for 96 h and control before preservation. Volcano plots for comparing (C) reperfusion after SCS for 96 h and immediately post-SCS for 96 h, and (D) reperfusion after ISC for 96 h and immediately post-ISC for 96 h. The volcano plots in (C) and (D) were normalized to immediately post-SCS and ISC, respectively. E) Downregulated metabolic processes from gene ontology with statistical differences ($-\log_{10}$ (adjusted p -value)) immediately after preservations compared to controls before preservation. F) Upregulated unfolded protein responses and heat responses from gene ontology with statistical differences ($-\log_{10}$ (adjusted p -value)) after reperfusion compared to immediately post-preservation. Dotted lines in E and F indicate the $p = 0.05$. G) Heat maps for metabolic processes including i) cholesterol, ii) fatty acid, and iii) glucose in control and immediately post-SCS and ISC for 96 h. H) Heat map for response to unfolded protein and I) apoptosis in control, immediately post-SCS and ISC for 96 h, after reperfusion in SCS and ISC for 96 h.

mimicking IRI. However, it is unclear why more IRI and lower barrier resistance were observed immediately post-ISC compared to SCS. The dominant mechanisms of injury and recovery between ISC and SCS likely differ during preservation and reperfusion processes. Despite lower metabolic activities in ISC, higher levels of inflammation and oxidative stress-related mRNA markers were observed in ISC. Although further studies are needed to clarify this, it has been reported that supercooled storage causes an increase in lipid peroxidation and a decrease in antioxidant capacity.^[54] To explore this further, lipidomic analysis in cell membranes at supercooling temperatures would be necessary as the next logical direction. Potentially, adding cell membrane stabilizers such as polyethylene glycol as a CPA in the storage solution could alleviate this problem.^[55]

A limitation of the study was the use of a single cell type, human coronary artery ECs, which might explain the discrepancy with clinical organ preservation timelines, where the preservation time limits for heart or VCAs are 4–6 h maximum with SCS. Although this study showed the capability of organ preservation protocols using vascular MPS, there is an obvious gap between the single cell type-based MPS and the real complex multicellular tissues. A more representative complex biomimetic model could be a potential direction for future research, focusing on the assessment of key features such as nitric oxide bioavailability, the release of adhesion molecules, and endothelial-derived hyperpolarization factors, which play major roles in maintaining endothelium integrity and function. Also, this model can be expanded to integrate with multi-compartment models whereby intricate cell-cell and cell-matrix interactions can be studied. Furthermore, given that microvascular systems can be more vulnerable to IRI than other vascular systems, further studies using a microvascular MPS that include other cell types such as stromal cells, pericytes, and fibroblasts in the *in vitro* model would enhance the correlation with clinical settings.^[56,57] Incorporating blood-like fluids can be a future direction to enhance the physiological relevance in terms of composition and viscosity. While this study investigated a single cooling and warming rate, optimizing these rates and ramp times could be an interesting future direction.

In conclusion, a multifunctional vascular MPS was developed to study organ preservation using variable WSS, EIS, and transcriptomic analysis. This system enabled real-time monitoring of endothelial barrier function and unbiased molecular-level analyses during preservation and reperfusion protocols. ISC showed better recovery of barrier resistance compared to SCS, with mRNA sequencing revealing related metabolic, protein unfolding, and inflammatory responses. These findings highlight the vascular MPS's capabilities for quantitative analysis of endothelial barrier function in organ preservation and reperfusion. Our work emphasizes the importance of the endothelium, suggesting that it requires special attention during organ preservation and development of new clinical protocols. Accordingly, the multifunctional vascular MPS testbed holds the potential to be expanded and adapted to evaluate a wide range of preservation protocols, thereby optimizing it for studies for extended organ storage. By leveraging its ability to simulate various physiological conditions and monitor responses at the molecular level, the MPS can provide valuable insights into the effectiveness of different preservation techniques, ultimately

enhancing the viability and longevity of stored organs for transplantation.

4. Experimental Section

MPS Fabrications: Vascular MPS was fabricated with soft lithography. Based on the WSS modeling, the mask was designed with AutoCAD (Autodesk Inc.) in Figure S2 (Supporting Information). Figure S1 (Supporting Information) illustrates the detailed schematics for Polydimethylsiloxane (PDMS) MPS fabrication. Patterned master wafer was fabricated via photolithography technique onto a 100 mm diameter silicon wafer (University Wafer). An SU8-2100 (Kayakum) photoresist was utilized, and this process involved spin coating, soft bake, UV exposure, and post-exposure bake, development, and hard bake. The surface of the master wafer was salinized using Trichloro (1H, 1H, 2H, 2H-perfluorooctyl) silane (Sigma) overnight. Electrode arrays for EIS measurements were fabricated with photolithography onto gold (100 nm)/titanium (5 nm) deposited glass substrates (Evaporated Metal Films). The placement of electrode pairs was designed to measure different WSS regions on the tapered microfluidics channel using AutoCAD (Figure S2, Supporting Information). A positive photoresist AZ-1504 (MicroChemicals) was used, and this process involved spin coating, soft bake, UV exposure, development, and lifting.

After thoroughly mixing a 10:1 ratio of PDMS (Dow Chemical, Sylgard 184) with a curing agent, the mixture was poured onto the master wafer mold and allowed to cure overnight at 70 °C before being peeled off. Then, a 0.75 mm diameter biopsy punch (Ted Pella) was used to punch holes into the inlet and outlet of the PDMS microfluidics channel. Lastly, oxygen plasma treatment was applied to attach PDMS onto electrode chips at 21 W for 24 seconds (98.8 sccm; 750 mTorr). The MPS devices were subsequently baked at 70 °C overnight to stabilize bonding and sterilized under UV exposure for at least 30 min before use. The alignment markers on inlet and outlet of electrodes (Figure S2, Supporting Information) were used to make the alignment between the PDMS channel and electrode arrays.

Fluid WSS Modeling: Computational modeling of the WSS and maximum fluid velocity was completed in COMSOL Multiphysics (COMSOL Inc.) using the imported AutoCAD geometry of the MPS system that was used to create the mask for soft lithography. Flow was assumed as laminar, using the no slip condition at the MPS walls, and the cell culture media perfused through the MPS was Newtonian with the fine finite element analysis mesh. The fluid was simulated at 37 °C to reflect the incubated conditions, with a dynamic viscosity of 0.84 mPa s. This value matches the viscosity of endothelial growth media provided by the manufacturer and is corroborated by experimental measurements elsewhere.^[39] The inlet boundary was modeled as the equivalent of 40 and 70 $\mu\text{L min}^{-1}$ of flow rate across the inlet cross-section. WSS was taken from the shear rate from the 3D velocity profiles created by COMSOL multiplied by the dynamic viscosity.

The previously reported tapered channels were assumed by the Hele-Shaw flow with a high aspect ratio (channel width/height = 50–293) and low Reynolds numbers.^[43,44] However, the chip was designed to decrease the aspect ratio in the channel to provide a 3D aspect in vasculature. The laminar flow was used in this modeling due to its lower aspect ratio (channel width/height = 3–23) and higher Reynolds number (0.62–3.75) than the designs in previous work. Figure 1C-ii shows that the laminar flow assumption in the design still offers a linear WSS with smaller than a 4% difference compared to when used in Hele-Shaw flow (Figure S3A, Supporting Information).

Cell Culture and Loading on MPS: Human coronary artery endothelial cells (Lonza) were cultured in Endothelial Cells Growth Medium MV (PromoCell) containing the supplements kit (PromoCell), maintained at 37 °C in a 5% CO₂ incubator. Vascular MPS was functionalized with 0.5 mg mL⁻¹ of fibronectin (Sigma) for 1 h at 37 °C before loading cells. A concentration of 30 million cells mL⁻¹ was loaded into the inlet of MPS using a pipette. After 2 h, 40 μL of media was added through inlet and outlet onto the chip and incubated overnight before applying flow. The cell loading and media exchange protocol was empirically optimized to allow ECs to attach to the walls of the device.^[58]

Perfusion: Pressure-driven pumps, flow sensor, and 2-Switch (Fluigent) were used for the perfusion setup (Figure S4, Supporting Information). Endothelial cells growth medium MV including 0.5 ng mL⁻¹ of human vascular endothelial growth factor 165 (Peprotech) was used for the perfusion media, which was recirculated using the 2-Switch setup. The 15 mL conical tubes for perfusion media were placed in a water bath at 37 °C. During the perfusion, MPS was placed in the incubation controlled of Lionheart microscope (Agilent) in 5% CO₂ at 37 °C. One day after loading ECs on the chip, the perfusion media was applied with 40 µL min⁻¹ for 6 h to the MPS after a linear increase of the flow rate from 0 to 40 µL min⁻¹ for 2 h.

EIS Measurements and Analysis: Impedance bode plots were measured ranging from 10 Hz to 1 MHz applied by 10 mV of AC voltage using the Gamry Interface 1010E (Gamry). Temporal impedance measurements were measured at 15 kHz every 30 seconds which is the most sensitive region based on Figure 3B. Bode plots for bare electrodes were measured after functionalization with fibronectin before loading the cells to calculate electrode resistance, constant phase element, and media resistance as a baseline with the equivalent circuit model (Figure S8B, Supporting Information). The downhill simplex method was utilized to fit the equivalent circuit models from Figures 3C and S8B (Supporting Information) using the Echem Analyst 2 Software (Gamry).^[59] Chi-squared was calculated as a sum of the weighted residuals to evaluate the goodness of fit. Figure S8C–F (Supporting Information) presents examples of equivalent circuit model fitting for the bare electrode and after cell loading onto the MPS. Figure 4A indicates when MPS were measured with EIS at 37 °C to quantify the tight junction quantification with circuit model fitting. For barrier R_{TJ} recovery rate after reperfusion (Figure 5J), the number of EIS measurements over 80% of normalized R_{TJ} after reperfusion (dotted line in Figure 5B) was counted.

Biopreservation Protocol: The biopreservation protocol of MPS with SCS and ISC is depicted in Figure 4A. The first protocol was SCS at 4 °C as the standard clinical practice, and the second one was ISC at -3 °C to investigate the effects of temperature and time on the preservation of endothelium. First, after MPS perfusion, the perfusion media was switched to room temperature PBS using a pipette. The MPS was cooled down from room temperature to 4 °C for SCS and 1 °C for ISC at ≈ 2 °C min⁻¹ using a chiller device (Cole-Parmer). Either at 1 or 4 °C, the University of Wisconsin preservation solution (Bridge to life), a commonly used clinical organ storage solution, was added to the MPS using a pipette. For ISC, MPS was carefully loaded onto the ISC chamber without any bubbles and cooled down to -3 °C using a 1 °C min⁻¹ rate. The electrode contact pads with soldering were coated with PDMS to minimize potential ice nucleation sites during ISC. For SCS, MPS was stored at 4 °C. After ISC preservation, MPS was warmed up from -3 to 1 °C at a rate of 1 °C min⁻¹ in ISC setup, followed by heating up to 21 °C at ≈ 2 °C min⁻¹ using the chiller. After SCS preservation, MPS was moved to the water chiller at 4 °C and warmed up to 21 °C at ≈ 2 °C min⁻¹. After heating up to room temperature from preservation, perfusion media was applied to MPS with 40 µL min⁻¹ flow rate for 4 h without gradual increment in 5% CO₂ at 37 °C to recapitulate reperfusion of blood after organ transplant.

Isochoric Supercooling Setup: In this study, a custom-built isochoric supercooling platform was employed to enable stable supercooling of the vascular MPS. The system, similar to the one described previously by Consiglio et al.,^[60] consists of a two-part isochoric chamber constructed from Al-7075. The chamber has a nominal internal volume of 20 mL, inner diameter of 1" and internal height of 1.75". A threaded tapered plug interfaces with the chamber body and forms a pressure-tight seal. The square exterior of the chamber interface with two thermoelectric elements that enable precise and responsive temperature control using a digital PID controller (TEC-1161-4A, Meerstetter Engineering GmbH, CH). A pressure transducer interfaces with the plug and enables low-latency monitoring of ice formation. In the event of freezing, expansion of ice within the rigid chamber generates a steep rise in pressure that can be resolved by the pressure transducer.^[61] All data shown here for ISC did not show a steep rise in pressure, an indicator for ice formation. The example of pressure curve is shown in Figure S18 (Supporting Information).

To mitigate the potential ice nucleation sites on the MPS, such as the interface between gold electrode or solder on the MPS contact pads and the UW solution, as well as the sharp edges of the glass substrate, a 10:1 ration of PDMS to curing agent was applied to these areas and cured at 70 °C overnight prior to use.

Immunofluorescence Images and Analysis for EC Morphology Quantification: The vascular MPS was rinsed in PBS, fixed in 4% paraformaldehyde (Millipore) for 15 min, and incubated overnight with 3% bovine serum albumin (Fisher) and 0.05% saponin (ThermoScientific) in PBS at 4 °C for permeabilization and blocking. For endothelial morphological and functional analysis with WSS, cells were stained for cadherin and VEGFR3 using the following antibodies: a) goat anti-VE-Cadherin (R&D Systems), b) mouse anti-vascular endothelial growth factor receptor 3 (VEGFR3) (R&D Systems) with 15 and 25 µg mL⁻¹, followed by overnight incubation at 4 °C. The secondary antibodies, AlexaFluor-488 anti-goat and AlexaFluor-647 anti-mouse (ThermoFisher), were used to stain VE-Cadherin and VEGFR3 with 1:250 dilution ratios, followed by a 4 h incubation at room temperature with 1 µg mL⁻¹ of DAPI (ThermoFisher) to stain the nucleus. For actin filament staining, 0.165 µM of rhodamine phalloidin (Invitrogen) was used, followed by incubation overnight at 4 °C with 1 µg mL⁻¹ DAPI. Between staining steps, the sample was washed with PBS three times for 5 min. Opera Phenix high content screening system (Perkin Elmer) and Lionheart Widefield Microscope (Agilent) were used for image acquisition.

CellProfiler was used to analyze EC morphology based on distinct WSS present in the vascular chip. Images were cropped to remove the edge of channels from the VE-Cadherin (Figure S6A, Supporting Information) to show only the EC monolayer with intensity recalculated to allow for thresholding (Figure S6B, Supporting Information). VE-Cadherin undergoes intensity inversion (Figure S6C, Supporting Information). Nuclei were identified using adaptive two-class Otsu thresholding with 0.1 arbitrary intensity units as minimum intensity on the DAPI layer (Figure S6D, Supporting Information). Cells were identified from primary object nuclei and subsequent adaptive two-class Otsu thresholding with propagation as the method to identify in CellProfiler (Figure S6E, Supporting Information). Once cells were mapped, properties of interest including cell area (pixels²), eccentricity, orientation (-90° to 90°, x-axis = 0°), and major/minor axes (pixels) were exported to Excel. Pixel-based units were corrected to microns using the microscopic scale, and orientation was corrected to make y-axis = 0°. Random cells' major axes were manually measured in ImageJ to check for agreement with CellProfiler. Poor agreement led to cell threshold setting adjustment of threshold correction and/or regularization factor until agreement was met. Statistical analysis was performed using the GraphPad Prism.

Transcriptomic Analysis: Four to seven independent replicates for vascular MPS were prepared for five different conditions including control, immediately post-SCS and -ISC for 96 h, and after 4 h of reperfusion in SCS and ISC for 96 h. ECs were dissociated from chips using TrypLE (Gibco) and collected by washing with PBS. RNeasy Mini Kit (Qiagen) was used to extract mRNAs from collected cells. The mRNA quality was assessed using the Agilent 2100 device (Agilent), and selected the samples with higher RNA integrity number than 4.0 and > 100 ng of amount. The NovaSeq X Plus (Illumina) was used for mRNA library preparation. Gene enrichment analysis was based on gene ontology and KEGG, including cholesterol metabolic process (GO:0008203), steroid metabolic process (GO:0008202), secondary alcohol metabolic process (GO:1902652), sterol metabolic process (GO:0016125), triglyceride metabolic process (GO:0006641), organic hydroxy compound metabolic process (GO:1901615), acylglycerol metabolic process (GO:0006639), neutral lipid metabolic process (GO:0006638), response to unfolded protein (GO:0006986), response to topologically incorrect protein (GO:0035966), protein refolding (GO:0042026), chaperone cofactor-dependent protein refolding (GO:0051085), 'de novo' posttranslational protein folding (GO:0051084), response to heat (GO:0009408), cellular response to heat (GO:0034605), response to temperature stimulus (GO:0009266), cellular response to oxidate stress (GO:0034599), MAPK signaling pathway (hsa04010), NF-kappa B signaling pathway (hsa04064), IL-17 signaling pathway (hsa04657), cytokine-cytokine receptor interaction (hsa04060), TNF signaling pathway (hsa04668), and apoptosis (hsa04210).

Gene set enrichment analysis was conducted using the GSEA software v.4.3.2^[62] with default parameters, applied to normalized count data via NovoMagic, an analysis platform by Novogene. The GSEA results were used to generate enrichment maps in Cytoscape software (Cytoscape Consortium). Nodes were included based on a false discovery rate (FDR) q-value cutoff of 0.75 and a P-value cutoff of 0.005. Edges cut-off was set to 0.375 and pathway cluster names were determined using Cytoscape's AutoAnnotate application. Clusters of interest were selected after manual examination of all individual nodes in clusters.

Statistical Analysis: The statistical analysis was performed by Prism software (GraphPad) and data were expressed as median ± quartiles in truncated violin plots with data points for Figures 2C,D,F, 4C–J, and 5A,B, Figures S11A, S12, and S13A,B (Supporting Information) and mean ± standard deviation in error bars for Figures 3B and S7A (Supporting Information). Number of replicates and details in statistical analysis were added to each Figure caption.

Supporting Information

Supporting Information is available from the Wiley Online Library or from the author.

Acknowledgements

This work was supported by the NSF Engineering Research Center for Advanced Technologies for Preservation of Biological Systems (ATP-Bio) NSF EEC #1941543. The authors would like to thank Dr. Berk Usta (Massachusetts General Hospital) for his helpful discussions.

Conflict of Interest

K.E.H. has a financial relationship with Organos Inc. A.N.C. and B.R. have a financial relationship with BioChoric Inc. and both they and the company may benefit from the commercialization of the results of this research. K.U. and B.E.U. have patent applications relevant to this field. K.U. and B.E.U. have financial interests in Sylvatica Biotech Inc. and K.U. serves on the Scientific Advisory Board for Sylvatica Biotech Inc., a private company developing high subzero organ preservation technologies.

Author Contributions

Y.K. and K.E.H. conceptualized the study. Y.K., I.G., and E.G. conducted the computational modeling analysis. Y.K., E.G., and S.R.M. developed the vascular MPS with electrical impedance sensing. A.N.C., J.V., and B.R. developed the isochoric supercooling system. Y.K. and E.G. conducted the experiment with vascular MPS for preservation studies. Y.K., I.G., E.G., S.R.M., G.N., B.W., A.A.A.A., B.W.E., I.F.R., K.U., B.E.U., K.E.H. analyzed the data. Y.K., E.G., A.N.C., and K.E.H. drafted the manuscript, and all authors edited it.

Data Availability Statement

The data that support the findings of this study are available from the corresponding author upon reasonable request.

Keywords

biopreservation, isochoric supercooling, electrical impedance spectroscopy, endothelial barrier function, microphysiological system

Received: October 29, 2024

Revised: January 18, 2025

Published online: February 19, 2025

- [1] D. P. Schladt, A. K. Israni, *Am. J. Transplant.* **2024**, *24*, S10.
- [2] D. L. Hoyert, J. Xu, *Natl. Vital Stat Rep.* **2012**, *61*, 1.
- [3] E. E. Guibert, A. Y. Petrenko, C. L. Balaban, A. Y. Somov, J. V. Rodriguez, B. J. Fuller, *Transfus. Med. Hemother.* **2011**, *38*, 125.
- [4] Ç. Duru, F. Biniyazan, N. Hadzimustafic, A. D'Elia, V. Shamoun, S. Haykal, *Front. Transplant.* **2023**, *2*, 1323387.
- [5] S. Giwa, J. K. Lewis, L. Alvarez, R. Langer, A. E. Roth, G. M. Church, J. F. Markmann, D. H. Sachs, A. Chandraker, J. A. Wertheim, M. Rothblatt, E. S. Boyden, E. Eidbo, W. P. A. Lee, B. Pomahac, G. Brandacher, D. M. Weinstock, G. Elliott, D. Nelson, J. P. Acker, K. Uygun, B. Schmalz, B. P. Weegman, A. Tocchio, G. M. Fahy, K. B. Storey, B. Rubinsky, J. Bischof, J. A. W. Elliott, M. Toner, *Nat. Biotechnol.* **2017**, *35*, 530.
- [6] A. Ward, D. K. Klassen, K. M. Franz, S. Giwa, J. K. Lewis, *Curr. Opin. Organ Transplant.* **2018**, *23*, 336.
- [7] D. H. Sachs, T. Kawai, M. Sykes, *Cold Spring Harb. Perspect. Med.* **2014**, *4*, a015529.
- [8] C. D. Lopez, A. O. Girard, I. V. Lake, B. C. Oh, G. Brandacher, D. S. Cooney, A. L. Burnett, R. J. Redett, *Nat. Rev. Urol.* **2023**, *20*, 294.
- [9] C. D. L. Ceresa, D. Nasralla, J.-M. Pollok, P. J. Friend, *Nat. Rev. Gastroenterol. Hepatol.* **2022**, *19*, 199.
- [10] M. Goutard, R. J. de Vries, P. Tawa, C. A. Pendexter, I. A. Rosales, S. N. Tessier, L. C. Burlage, L. Lantieri, M. A. Randolph, A. G. Lellouch, C. L. Cetrulo, Jr., K. Uygun, *J Reconstr. Microsurg.* **2023**, *39*, 350.
- [11] M. J. Taylor, B. P. Weegman, S. C. Baicu, S. E. Giwa, *Transfus. Med. Hemother.* **2019**, *46*, 197.
- [12] Y. Berkane, J. Hayau, I. Filz von Reiterdank, A. Kharga, L. Charlès, A. B. Mink van der Molen, J. H. Coert, N. Bertheuil, M. A. Randolph, C. L. Cetrulo, A. Longchamp, A. G. Lellouch, K. Uygun, *Front. Transplant.* **2023**, *2*, 1269706.
- [13] R. J. de Vries, S. N. Tessier, P. D. Banik, S. Nagpal, S. E. J. Cronin, S. Ozer, E. O. A. Hafiz, T. M. van Gulik, M. L. Yarmush, J. F. Markmann, M. Toner, H. Yeh, K. Uygun, *Nat. Biotechnol.* **2019**, *37*, 1131.
- [14] S. N. Tessier, R. J. de Vries, C. A. Pendexter, S. E. J. Cronin, S. Ozer, E. O. A. Hafiz, S. Raigani, J. P. Oliveira-Costa, B. T. Wilks, M. Lopera Higuaita, T. M. van Gulik, O. B. Usta, S. L. Stott, H. Yeh, M. L. Yarmush, K. Uygun, M. Toner, *Nat. Commun.* **2022**, *13*, 4008.
- [15] Z. Han, J. S. Rao, L. Gangwar, B.-E. Namsrai, J. L. Pasek-Allen, M. L. Etheridge, S. M. Wolf, T. L. Pruett, J. C. Bischof, E. B. Finger, *Nat. Commun.* **2023**, *14*, 3407.
- [16] L. Zhan, J. S. Rao, N. Sethia, M. Q. Slama, Z. Han, D. Tobolt, M. Etheridge, Q. P. Peterson, C. S. Dutcher, J. C. Bischof, E. B. Finger, *Nat. Med.* **2022**, *28*, 798.
- [17] L. I. Mazilescu, C. Parmentier, S. N. Kalimuthu, S. Ganesh, M. Kawamura, T. Goto, Y. Noguchi, M. Selzner, T. W. Reichman, *Am. J. Transplant.* **2022**, *22*, 1339.
- [18] Y. Berkane, I. Filz von Reiterdank, P. Tawa, L. Charlès, M. Goutard, A. T. Dinicu, M. Toner, N. Bertheuil, A. B. Mink van der Molen, J. H. Coert, A. G. Lellouch, M. A. Randolph, C. L. Cetrulo, K. Uygun, *Sci. Rep.* **2024**, *14*, 12618.
- [19] I. Filz von Reiterdank, P. Tawa, Y. Berkane, E. de Clermont-Tonnerre, A. T. Dinicu, C. Pendexter, M. Goutard, A. G. Lellouch, A. B. Mink van der Molen, J. H. Coert, C. L. Cetrulo Jr., K. Uygun, *Cryobiology* **2024**, *116*, 104950.
- [20] M. J. Powell-Palm, V. Charwat, B. Charrez, B. Siemons, K. E. Healy, B. Rubinsky, *Commun. Biol.* **2021**, *4*, 1118.
- [21] T. A. Berendsen, B. G. Bruinsma, C. F. Puts, N. Saeidi, O. B. Usta, B. E. Uygun, M.-L. Izamis, M. Toner, M. L. Yarmush, K. Uygun, *Nat. Med.* **2014**, *20*, 790.
- [22] H. Huang, M. L. Yarmush, O. B. Usta, *Nat. Commun.* **2018**, *9*, 3201.
- [23] Filz von Reiterdank I, Taggart MS, McCarthy ME, Dinicu AT, Uygun BE, Coert JH, Mink van der Molen AB, Uygun K. Enhanced VCA Storage: A Pilot Study Demonstrating Supercooling in Orthotopic Rodent Hindlimb Transplantation. *Transplant Proc*, **2024**, *56*, 2039–2045.

- [24] Filz von Reiterdank I, Dinicu AT, Rosales I, Cetrulo CL Jr, Coert JH, Mink van der Molen AB, Uygun K. Supercooling preservation of vascularized composite allografts through CPA optimization, thermal tracking, and stepwise loading techniques. *Sci Rep* **2024**, *14*, 22339.
- [25] M. J. Powell-Palm, E. M. Henley, A. N. Consiglio, C. Lager, B. Chang, R. Perry, K. Fitzgerald, J. Daly, B. Rubinsky, M. Hagedorn, *Nat. Commun.* **2023**, *14*, 4859.
- [26] K. A. Murray, M. I. Gibson, *Nat. Rev. Chem.* **2022**, *6*, 579.
- [27] B. P. Best, *Rejuvenation Res.* **2015**, *18*, 422.
- [28] M. J. Powell-Palm, A. Koh-Bell, B. Rubinsky, *Appl. Phys. Lett.* **2020**, *116*, 123702.
- [29] S. Browne, E. L. Gill, P. Schultheiss, I. Goswami, K. E. Healy, *Stem Cell Rep.* **2021**, *16*, 2058.
- [30] C. A. Pendexter, O. Haque, M. Mojoudi, S. Maggipinto, M. Goutard, S. Baicu, A. G. Lellouch, J. F. Markmann, G. Brandacher, H. Yeh, S. N. Tessier, C. Cetrulo, K. Uygun, *PLoS One* **2023**, *18*, e0266207.
- [31] A. Meyers, S. Pandey, V. Koppaarthi, P. Sadeghi, R. C. Clark, B. Figueroa, S. Dasarathy, H. Brunengraber, F. Papay, A. Rampazzo, B. Bassiri Gharb, *Artif. Organs* **2023**, *47*, 290.
- [32] M. Y. Kim, H. Y. Yoon, S. Lee, *Transplant Proc.* **2021**, *53*, 1756.
- [33] S. N. Tessier, L. Weng, W. D. Moyo, S. H. Au, K. H. K. Wong, C. Angraseuth, A. E. Stoddard, C. Lu, L. T. Nieman, R. D. Sandlin, K. Uygun, S. L. Stott, M. Toner, *ACS Biomater. Sci. Eng.* **2018**, *4*, 3006.
- [34] M. A. J. Zieger, M. P. Gupta, M. Wang, *BMC Genomics* **2011**, *12*, 630.
- [35] W. J. Polacheck, M. L. Kutys, J. Yang, J. Eyckmans, Y. Wu, H. Vasavada, K. K. Hirschi, C. S. Chen, *Nature* **2017**, *552*, 258.
- [36] K. Haase, F. Piatti, M. Marcano, Y. Shin, R. Visone, A. Redaelli, M. Rasponi, R. D. Kamm, *Biomaterials* **2022**, *280*, 121248.
- [37] Y. Qiu, B. Ahn, Y. Sakurai, C. E. Hansen, R. Tran, P. N. Mimche, R. G. Mannino, J. C. Ciciliano, T. J. Lamb, C. H. Joiner, S. F. Ofori-Acquah, W. A. Lam, *Nat. Biomed. Eng.* **2018**, *2*, 453.
- [38] B. W. Ellis, G. Ronan, X. Ren, G. Bahcecioglu, S. Senapati, D. Anderson, E. Handberg, K. L. March, H.-C. Chang, P. Zorlutuna, *Small* **2022**, *18*, 2201330.
- [39] V. S. Shirure, C. C. W. Hughes, S. C. George, *Annu. Rev. Biomed. Eng.* **2021**, *23*, 141.
- [40] J. Yeste, M. García-Ramírez, X. Illa, A. Guimerà, C. Hernández, R. Simó, R. Villa, *Lab Chip* **2018**, *18*, 95.
- [41] J. A. Stolwijk, K. Matrougui, C. W. Renken, M. Trebak, *Pflügers Archiv – Europ. J. Physiol.* **2015**, *467*, 2193.
- [42] P.-A. Doriot, P.-A. Dorsaz, L. Dorsaz, E. De Benedetti, P. Chatelain, P. Delafontaine, *Coronary Artery Dis.* **2000**, *11*, 495.
- [43] S. Usami, H.-H. Chen, Y. Zhao, S. Chien, R. Skalak, *Ann. Biomed. Eng.* **1993**, *21*, 77.
- [44] F. Karimi, V. J. Thombare, C. A. Hutton, A. J. O'Connor, G. G. Qiao, D. E. Heath, *J. Biomed. Mater. Res., Part A* **2021**, *109*, 313.
- [45] N. Baeyens, S. Nicoli, B. G. Coon, T. D. Ross, K. Van den Dries, J. Han, H. M. Lauridsen, C. O. Mejean, A. Eichmann, J.-L. Thomas, J. D. Humphrey, M. A. Schwartz, *eLife* **2015**, *4*, e04645.
- [46] S. Noria, F. Xu, S. McCue, M. Jones, A. I. Gotlieb, B. L. Langille, *Am J Pathol* **2004**, *164*, 1211.
- [47] N. Sakamoto, N. Saito, X. Han, T. Ohashi, M. Sato, *Biochem. Biophys. Res. Commun.* **2010**, *395*, 264.
- [48] S. Holm, T. Holm, Ø. G. Martinsen, *PLoS One* **2021**, *16*, e0248786.
- [49] L. Banci, F. Camponeschi, S. Ciofi-Baffoni, R. Muzzioli, *J. Am. Chem. Soc.* **2015**, *137*, 16133.
- [50] C. Hetz, K. Zhang, R. J. Kaufman, *Nat. Rev. Mol. Cell Biol.* **2020**, *21*, 421.
- [51] P. Walter, D. Ron, *Science* **2011**, *334*, 1081.
- [52] A.-R. Biglarnia, M. Huber-Lang, C. Mohlin, K. N. Ekdahl, B. Nilsson, *Nat. Rev. Nephrol.* **2018**, *14*, 767.
- [53] G. Strandberg, C. M. Öberg, A. M. Blom, O. Slivca, D. Berglund, M. Segelmark, B. Nilsson, A.-R. Biglarnia, *Kidney Int. Rep.* **2023**, *8*, 2592.
- [54] Z. Isiksacan, N. William, R. Senturk, L. Boudreau, C. Wooning, E. Castellanos, S. Isiksacan, M. L. Yarmush, J. P. Acker, O. B. Usta, *Commun. Biol.* **2024**, *7*, 765.
- [55] H. Chen, B. W. Ellis, A. T. Dinicu, M. Mojoudi, B. T. Wilks, S. N. Tessier, M. Toner, K. Uygun, B. E. Uygun, *Cryobiology* **2024**, *116*, 104926.
- [56] X. Jiang, Y. K. Sung, W. Tian, J. Qian, G. L. Semenza, M. R. Nicolls, *J. Mol. Med.* **2014**, *92*, 797.
- [57] H. Xu, J. X. Zhang, J. W. Jones, J. H. Southard, M. G. Clemens, C. Y. Lee, *Transplant Proc.* **2005**, *37*, 335.
- [58] I. Goswami, Y. Kim, G. Neiman, B. Siemons, J. I. Velazquez, K. Yazgan, T. Ng, K. E. Healy, *bioRxiv* **2025**, *8*, 632020.
- [59] J. A. Nelder, R. Mead, *Comput. J.* **1965**, *7*, 308.
- [60] A. N. Consiglio, D. Lilley, R. Prasher, B. Rubinsky, M. J. Powell-Palm, *Cryobiology* **2022**, *106*, 91.
- [61] M. J. Powell-Palm, *RSC Adv.* **2022**, *12*, 20603.
- [62] A. Subramanian, P. Tamayo, V. K. Mootha, S. Mukherjee, B. L. Ebert, M. A. Gillette, A. Paulovich, S. L. Pomeroy, T. R. Golub, E. S. Lander, J. P. Mesirov, *Proc. Natl. Acad. Sci. U. S. A.* **2005**, *102*, 15545.